

Fabrication of highly conductive graphene flexible circuits by 3D printing



Di Zhang^a, Baihong Chi^c, Bowen Li^a, Zewen Gao^a, Yao Du^a, Jinbao Guo^a, Jie Wei^{b,a,*}

^a College of Materials Science and Engineering, Beijing University of Chemical Technology, No.15, Bei San Huan East Road, Chao Yang District, Beijing, China

^b Beijing Engineering Research Center for the Synthesis and Applications of Waterborne Polymers, Beijing 100029, China

^c College of Mechanical and Electrical Engineering, Beijing University of Chemical Technology, No.15, Bei San Huan East Road, Chao Yang District, Beijing, China

ARTICLE INFO

Article history:

Received 25 December 2015

Received in revised form 5 March 2016

Accepted 11 March 2016

Available online xxx

Keywords:

3D print

Graphene

Flexible circuits

ABSTRACT

Fused depositing modeling (FDM) is a fast, efficient process among 3D printing techniques. In this paper, we report the fabrication of the 3D printed flexible circuits based on graphene. Modified two-step in-situ reduced method is used to synthesize reduced graphene oxide (r-GO), whose conductivity can reach to 600 S/cm. Polylactic acid (PLA) and r-GO are mixed by melt blending. The SEM images show that the r-GO can be homogenous dispersed in the PLA. The 3D print-used composites filaments with the diameter of 1.75 mm are fabricated through melt extrusion. The conductivity of the composite filaments from 3D printer can reach to 4.76 S/cm (6 wt% r-GO). The orientation of r-GO occurs during the extrusion process, which contributing to increase the conductivity of the filaments. The composite also exhibit superior mechanical property. The printed 2D and 3D flexible circuits have strong interface bonding force between the layers. The filaments from 3D printer can replace the copper wire because of the high conductivity. This arbitrary 3D graphene-based structure printing technic may open a new prospect in electronic and energy storage fields.

© 2016 Elsevier B.V. All rights reserved.

1. Introduction

Organic electronic devices, such as fuel cell, solar cell, supercapacitor, sensor, etc, have been greatly updating in the laboratory-scale research during the past few decades. Even so, finding a fast and cost-effective method for fabricating high conductive flexible circuit is the main barrier before closing the gap between laboratory-scale research and industrial application. It is quite challenging to establish a system which combining cost-effective and high-performance materials with fast and scalable micro-fabrication technology. We and others have done a lot of work to fabricate micro or nano flexible circuit. Innovative technique including nanoimprinting [1], screen printing [2], dip-pen lithography [3], micro contact printing [4], inkjet printing [5], etc., have been used. However, all these method can barely be applied to practical scalable production because of the small amount, expensive materials or the slow, unstable fabricating process. The state-of-the-art micro-fabrication technology is lightscribe [6], in which the laser from a DVD drive was used to precisely reduce the graphene oxide (GO) film on the disc, then the

circuits of reduced graphene oxide (r-GO) were formed. The principal weakness of this latest technique lies in the poor physical properties of r-GO reduced by the high temperature laser, which can be proved by the fact that this kind of circuit can be applied to strain sensor [7]. The discovery of graphene in 2004 terminated the longstanding debate on purely two-dimension materials. Because of its unique structure and remarkable properties [8], graphene has been applying to any fields we can imagine. In terms of organic electronic field, many researchers have successfully implemented graphene or polymer-graphene composites into lithium ion batteries [9], supercapacitors [10], solar cell [11] and sensors [12] so forth. However, recently some authoritative researchers have raised doubts on this 'graphene fever'. They thought that all the previous data of graphene-based electrochemical energy-storage devices (EESD) are not real breakthrough. Due to various reasons, graphene still cannot replace the currently wide-used carbonous materials. They appeal that more work should be done aiming at practical application so that we can clarify whether graphene can meet the market's performance requirements [13]. The doubts from these authoritative researchers may possible bring a pause on graphene-based EESD research, retrieving our thought back to the pristine but wide practical properties of graphene such as high electrical and thermal conductivity.

* Corresponding author.

E-mail addresses: weij@mail.buct.edu.cn, weijie-2008@hotmail.com (J. Wei).

3D printing has brought a revolution to materials manufacturing industry because its additive manufacture technology broke the traditional manufacturing mode [14]. 3D printing has been widely applied in electronics [15] chemistry [16], physics [17], tissue engineering [18] and other fields [19] since arbitrary 3D structures can be fabricated. But few reports combine chemistry with 3D printing. Fused deposition modeling (FDM) is the most common used technique among 3D printing technologies, in which the 3D structure is established by extruding materials layer-by-layer through the capillary nozzles, thus allowing various kinds of materials used in FDM. In this report, we used the modified two step in-situ reduced method [20] to synthesize the high-conductive graphene, whose conductivity can reach to 600 S/cm, as the filler of PLA. PLA and graphene are homogeneously mixed by melt blending, after which graphene can be well dispersed in the PLA substrate. Then the composites were processed to fabricate the composite filament with the diameter of 1.75 mm, which is the material of 3D printer. We printed the 2D flexible circuits on different substrates. The composite circuits have a strong interface bonding force with the substrate, and the filaments from the 3D printer exhibit conductivity up to 4.76 S/cm (6 wt%). We have proved that the graphene had a process of orientation during the deposition, that is, the extrusion process. The orientation of graphene will help to improve the conductivity of the composite. The 3D flexible circuits exhibit good bonding force between layers, indicating that the 3D structure can maintain the same good mechanical property in both axial direction and transverse direction.

The materials used, both PLA and graphene, can be massive produced in a cheap way, demonstrating that the whole experimentation can be well transferred in practical application. Fig. 1 shows the process of graphene-based 3D printing in this report. As far as we know, this is the first time to use the PLA-graphene composite to print flexible circuits. The whole graphene-based 3D manufacturing process in this report will have a wide potential application [25] and may bring a new prospect in electronic and energy storage field.

2. Experimental

2.1. Materials

The natural graphite flakes were purchased from Shenzhen Nanotechnologies Co., Ltd. All the chemical reagents in the modified Hummers method were purchased from Sinopharm Chemical Reagent Beijing Co., Ltd. The 4-iodoaniline was purchased from Tokyo Chemical Industry. PLA was purchased from MakerBot, America. All chemical reagents are analytically pure and used without further purification.

2.2. Modified two step in-situ reduce method of synthesizing high conductive graphene

GO was synthesized by the modified Hummers method [21]. Then the GO was first chemical reduced by 4-iodoaniline: 0.05 g GO was dissolved in 100 ml concentrated sulfuric acid (98% H_2SO_4) and ultrasonicated for 30 min. Move the solution to a flask, slowly add 1.8 g 4-iodoaniline and 0.69 g NaNO_2 to the flask and keep stirring for 1 h at 60 °C. After cooling, wash the product by DMF and ethyl alcohol until colourless, then vacuum-dried for 24 h at 60 °C. The second reduction of GO is thermal reduction: put the first chemical reduced GO (c-r-GO) in a corundum boat and put it in the tube furnace at 1050 °C for 1 h under the argon atmosphere. If needed, all the quantities above can be multiplied.

2.3. Fabrication of the 3D-print used composite filament

The threadlike PLA were smashed by a pulverizer, then the smashed PLA and second thermal reduced graphene (t-r-GO) were put together into the HAAKE twin-screw melt mixer, the operation temperature and time is 160 °C and 15 min, respectively, and the screw revolving speed is 80 r/min. The produced composite was cut into pieces before cooling, then smashed them into powder by a pulverizer. A mini single screw extruder was used to transfer the composite powder to the filaments with the diameter of 1.75 mm.

2.4. Fabrication of the 2D and 3D flexible circuits

The 2D or 3D flexible circuit were designed by MakerBot or other three dimensional design software. Different substrate-paper, polyimide (PI) film-were put in the platform (X–Y plane) and fasten tightly, then circuits were printed on them. The 3D flexible circuits were printed directly in the platform. The heating temperature of the 3D printer is 210 °C. The PI film were soaked in the H_2O_2 – H_2SO_4 solution (volume ratio 1:3) for 12 h beforehand.

2.5. Mechanical test and electronic test

The stretching test bars with different graphene ratio (t-r-GO) were printed. Five test bars of every graphene ratio were stretched. The average size of the stretch cross section is 5.4 mm × 2.05 mm, the stretching speed is 50 mm/min. The Young's modulus was determined by using a 0.2% strain offset linear slope method. The fore-probe method was used to measure the conductivity of the wafer samples. Two-point method was used to measure the conductivity of the filaments through the equation: $R = L/\sigma S$, where R is the resistance of the sample, L and S are the length and the cross sectional area of the filament, respectively, and σ is the conductivity of the sample.

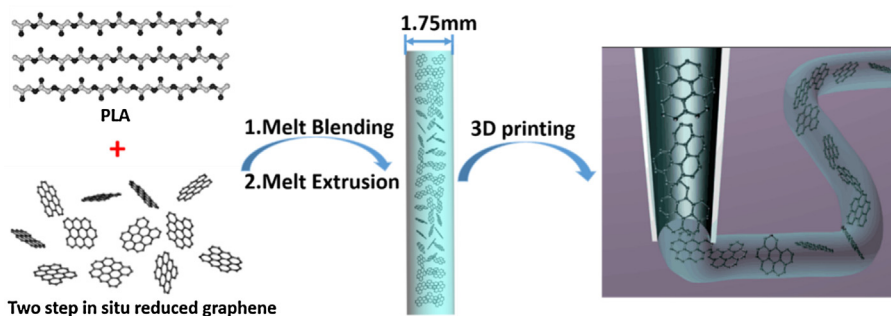


Fig. 1. Simplified schematics depicting the process of graphene-based 3D printing using the technique of FDM.

2.6. Measurements

FT-IR spectrophotometer (PerkinElmer Spectrum RX1, America) was used to characterize the oxygen-containing functional groups on the graphite sheets. The crystallinity and the defects of the graphite sheets were characterized by X-ray diffraction (XRD, Rigaku D/Max2500 VB2+pc, Japan). The defects of the graphite sheets are characterized by Raman spectra (Renishaw in Via, UK) with a laser of 514 nm and recorded on solid samples. The element contents were analyzed by X-ray photoelectron spectroscopy (XPS, ESCALAB 250, Thermo VG, America). The morphology and surface chemistry of the GO or r-GO and the PLA-graphene composites were characterized by scanning electron microscopy (SEM, Hitachi S-4700, Japan) and high-resolution transmission electron microscopy (HRTEM, JEOL TEM-3010, Japan). PLA and synthesized graphene were melt blended by twin-screw HAAKE melt mixer (HAAKE Rheomex OS, Thermo Sci., America). The micro extruder used was assembled in our lab, the screw diameter is 18 mm (18 mm × 20 mm) and the extrusion head diameter is 1.75 mm. The spray nozzle diameter of the 3D printer (Makerbot Replicator 2, America) was 400 μm. The mechanical tests were operated by universal materials testing machine (Shimadzu SBL-1KN, Japan). We use the four probe method ($\geq 10^{-5}$ S cm $^{-1}$, Baishen Technologies Co., Ltd., SX1934, China) and two-point method ($< 10^{-5}$ S cm $^{-1}$, Guilin Electrical Equipment Scientific Research Institute Co., Ltd., PC 68 digital high resistance meter, China) to measure the conductivity or the resistance of the samples.

3. Results and discussion

3.1. Characterizations of two-step reduced method for synthesizing r-GO

Fourier transform infrared (FT-IR) was performed on GO, first chemical reduced GO (c-r-GO) and the second thermal reduced GO (t-r-GO), in order to demonstrate the superior properties of the two-step reduced graphene, the thermal reduced GO (r-GO) was also measured as the control group (Fig. 2(a)). In Fig. 2(a), the characteristic peaks appear in 1062 cm $^{-1}$ (C–O in ether), 1224 cm $^{-1}$ (hydroxyl C–OH stretching), 1387 cm $^{-1}$ (O–H in hydroxyl) and 1723 cm $^{-1}$ (C=O stretching vibration), which are

the chemical bonding of the oxygen-containing functional groups on the graphite sheets. In addition, the peaks between 3400 cm $^{-1}$ and 3500 cm $^{-1}$ are due to the water in the sample. These characteristic peaks are obvious in GO line, because the graphite sheets of GO have many oxygen-containing functional groups after strong oxidation from nature graphite. But in the lines of c-r-GO and r-GO, these peaks become weaker or even disappear, confirming that quite amount of oxygen-containing functional groups are reduced during chemical reduction or thermal reduction. On the other hand, it is hard to see any difference of peak intensity between the lines of c-r-GO and r-GO, indicating that the effect of 4-iodoaniline reduction and thermal reduction to GO are almost the same. There is no clear characteristic peaks in the line of t-r-GO, providing evidence that after two-step reduction, the oxygen-containing functional groups are almost disappear. As we all know, the ultra-high conductivity of graphene is due to the sp 2 orbital hybridization of the atomic-scale carbon hexagonal pattern, the free-moving electrons can shuttle smoothly via the half-filled band constituted by π -bands and π^* -bands [22]. But the introduction of the oxygen-containing functional groups break the conjugated structure thus sharply lower the conductivity of the graphite sheets. In view of the above discussed, it is visualized in the FT-IR pattern that the conductivity of the t-r-GO are much higher than c-r-GO and r-GO.

The XRD diffraction pattern of graphite, GO, c-r-GO and t-r-GO is showed in Fig. 2(b), we can see that graphite shows an intense peak at 26.52°. Then it can be calculated through the Bragg equation that the interlayer spacing of graphite is 0.335 nm. The GO, c-r-GO and t-r-GO show the characteristic peaks in 10.07°, 24.26° and 26.26°, respectively. Similarly, the interlayer spacing of GO, c-r-GO, t-r-GO are 0.877 nm, 0.367 nm, 0.339 nm, respectively. The interlayer spacing of GO reach to 0.877 nm from 0.335 nm (graphite) is due to the insertion of the oxygen-containing functional groups between the graphite layers. After the chemical reduction, the interlayer spacing of c-r-GO decreased to 0.367 nm, this is because parts of the oxygen-containing functional groups have been reduced and the reduced parts has a different interlayer distance from the unreduced parts. It is worth noting that the interlayer spacing of t-r-GO is 0.339 nm, which is very close to the graphite, indicating that there is almost no oxygen-containing functional groups on the sheets of t-r-GO. This phenomenon is

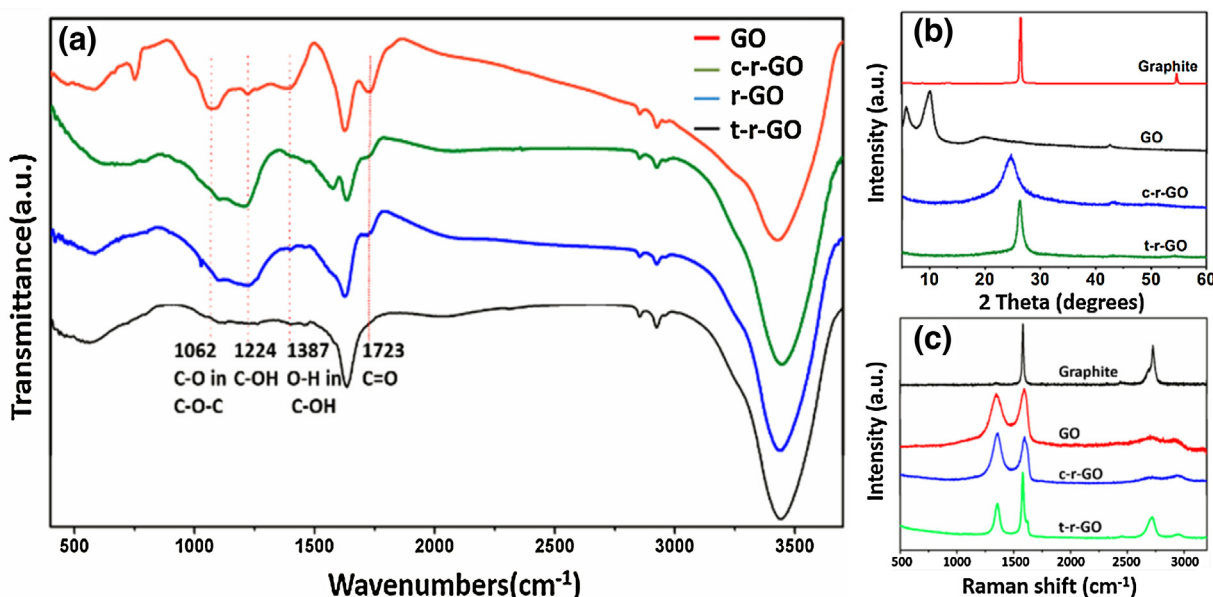


Fig. 2. FT-IR pattern (a), XRD pattern (b) and Raman spectra (c) of the two-step reduced method for synthesizing graphene.

consistent with the results of the FT-IR, further demonstrating the superior conductivity of t-r-GO.

These four samples show D band in around 1353 cm^{-1} and G band in around 1580 cm^{-1} in Raman spectra (Fig. 2(c)). The ratio of the D band intensity and G band intensity (I_D/I_G) represents the defected extent of materials [23]. On the carbon hexagonal lattice, I_D/I_G corresponding to the hybridization area of sp^3/sp^2 . So the I_D/I_G of pristine graphite (0.11) was calculated for the comparison purpose. Such a low I_D/I_G implying the high integrity of the graphite lattice. Then the D band of GO is much stronger than that of graphite. The I_D/I_G of GO (1.32) increases dramatically compared with that of pristine graphite, confirming that the introduction of the oxygen-containing functional groups bring quite an amount of structural disorder in the graphitic sheets. And the oxidation process break the delocalized bond of aromatic structure. After chemical reduction, the I_D/I_G value of c-r-GO keep increasing to 1.51. Based on the previous work [24], we believe that although the total sp^2 hybridization area has been increased after reduction, the average size of the sp^2 domains has become smaller, resulting in the I_D/I_G further increased. After secondary thermal reduction, it is obviously that the D band of t-r-GO decreased, and the I_D/I_G of t-r-GO also sharply decreased to 0.67. This change of the I_D/I_G demonstrating that during the secondary thermal reduction, the smaller sized sp^2 domains coalesce together, that is to say, the sp^3 gaps among the sp^2 domains disappear, the carbon lattice nearly recover to its original hexagonal sp^2 hybridization state with few defects. So the Raman spectra from GO to the final t-r-GO indicating that the chemical reduction to GO can remove quite a part of the oxygen-contained functional groups, but the chemical reduction extent can only reach to a choke point, which is not enough to cause the I_D/I_G decrease comparing with GO. But after high temperature thermal reduction, the sp^2 domains coalesce together, once again forming the sp^2 hybridization carbon lattice. This may explain the fact that the conductivity of the thermal reduced graphene is higher than the chemical reduced ones.

The XPS was used to analyze the elements contents. Fig. 3 and Table S1 show the C 1s spectra and the calculated C/O ratio of graphite, GO, c-r-GO and t-r-GO. It can be seen that the peak of C—C, C=C appear in near 284.9 eV in the all four samples, which represents the carbon skeleton of the hexagonal pattern of graphite sheets. The peaks of C—O, C=O, O—C=O appear in near 286.7 eV, 287.5 eV and 289.5 eV, respectively. It is worth noting that in Fig. 3(c), the peak of C—I appears in near 285.4 eV, and the iodine content is 2.96% in c-r-GO, which is due to that some 4-iodoaniline were grafted to the surface of graphite sheets after the chemical reduction. As we can see in Table S1, the oxygen content of GO is much higher than that of graphite. Then after two-step reduction, the oxygen content decrease gradually. The oxygen content of the finally t-r-GO decrease to 3.17%, which means that most oxygen-containing functional groups were reduced after the two-step reduction. The results of XPS are totally consistent with the FTIR, XRD and Raman results.

3.2. Morphology and mechanical tests

The TEM and SEM are used to characterize the morphology of t-r-GO and the PLA-t-r-GO composite (Fig. 4). Fig. 4(a and b) shows the TEM images of synthesized t-r-GO, from which we can see the monolayer of graphene clearly, which means the graphite sheets were well exfoliated during the fabricating process. The wide-spread monolayer graphene also reflects the high conductivity of graphene. In both of the TEM pictures, the typical ripples and folds of monolayer graphene were showed, which provide a large superficial surface for the further integration with PLA. A perfect hexagonal lattice diffraction points was exhibited in the inset SAED pattern, confirming the monolayer structure of synthesize t-r-GO. The synthesized t-r-GO exhibit the conductivity up to 600 S/cm. Then we have insured that the PLA and graphene were homogeneous blended in the HAAKE mixer. Fig. S1 shows the parameters during the melt blending process. Fig. 4(c and d) show the SEM cross section pictures of PLA-t-r-GO from HAAKE mixer, in which

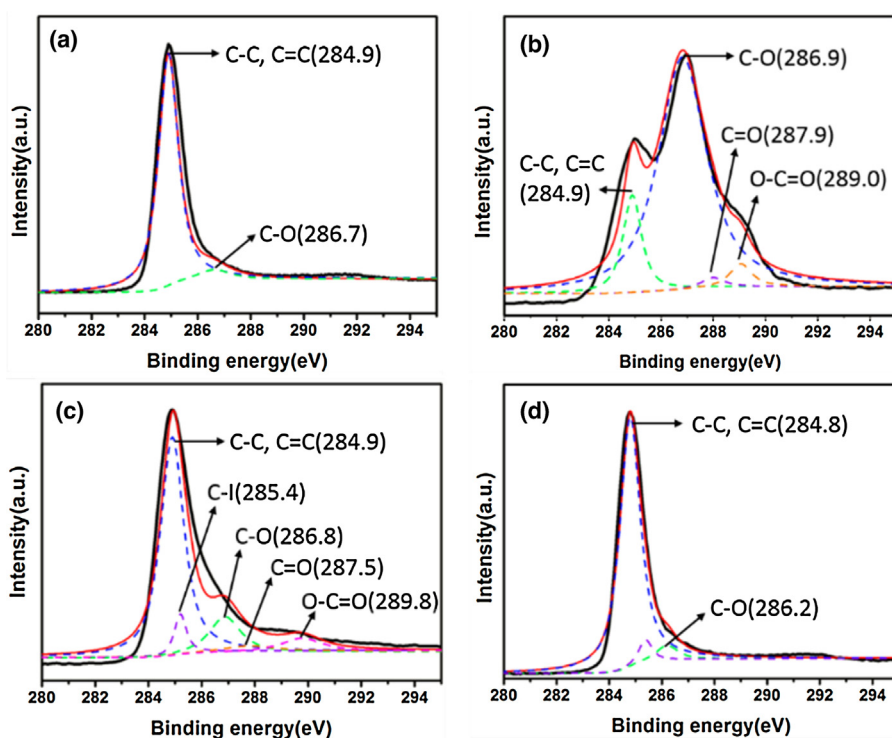


Fig. 3. XPS pattern of (a) graphite, (b) GO, (c) c-r-GO, (d) t-r-GO.

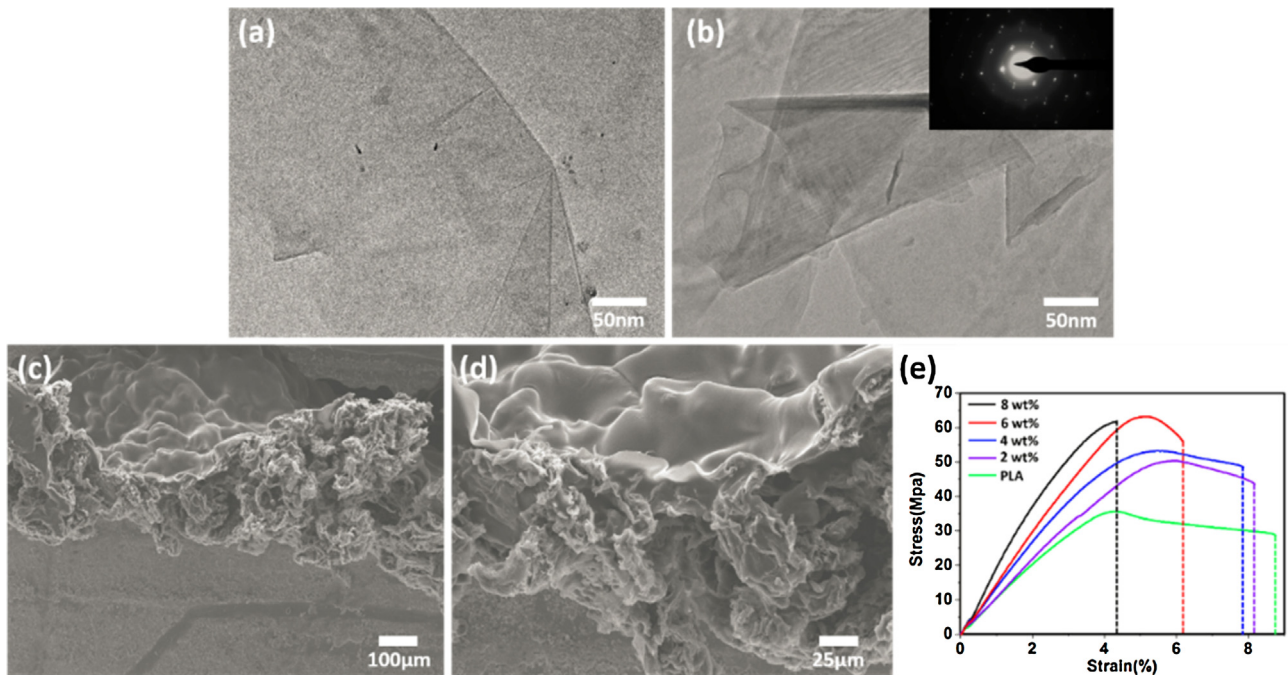


Fig. 4. (a and b) TEM images of t-r-GO, and the inset is the corresponding selected area electron diffraction (SAED), (c and d) SEM cross section images of PLA-t-r-GO, (e) Static mechanical properties tests (stress versus strain) of 3D printed PLA-graphene composites with different graphene weight ratio.

the outside surface of PLA-t-r-GO is smooth, implying that the synthesized t-r-GO are well wrapped by PLA. In the fracture surface, we can see the bedding-plane cleavage structure which was created by the homodisperse of the t-r-GO. And the wrinkled layers of t-r-GO can be clearly observed. Besides, it is indistinct to see the interface between PLA and t-r-GO, indicating that the interface bonding force between the substrate and fillers are very strong, and the t-r-GO are well wrapped and covered by PLA. The good dispersing and the strong interface bonding force may contribute to improve the conductivity of the composite.

We printed the tensile test bars with different graphene weight ratio. Fig. 4(e) shows the results. When the graphene weight ratio

reach to 8%, the tensile bar will have a brittle fracture. The Young's modulus and the tensile strength will increase with the growth of the graphene weight ratio while the elongation will decrease. The elongation of the pure PLA can reach to 8.79%. The addition of graphene will help to increase the Young's modulus of pure PLA, thus strengthen the mechanical properties of the composite. Table S2 shows the detail numerical value of the mechanical properties.

The Young's modulus and the tensile strength of the PLA-graphene here are higher than other 3D printed graphene composite reported before [25]. When the graphene weight ratio reach to 8%, the brittle fracture will occur, implying that the rigidity of the composite is too high. So we choose the composite with the

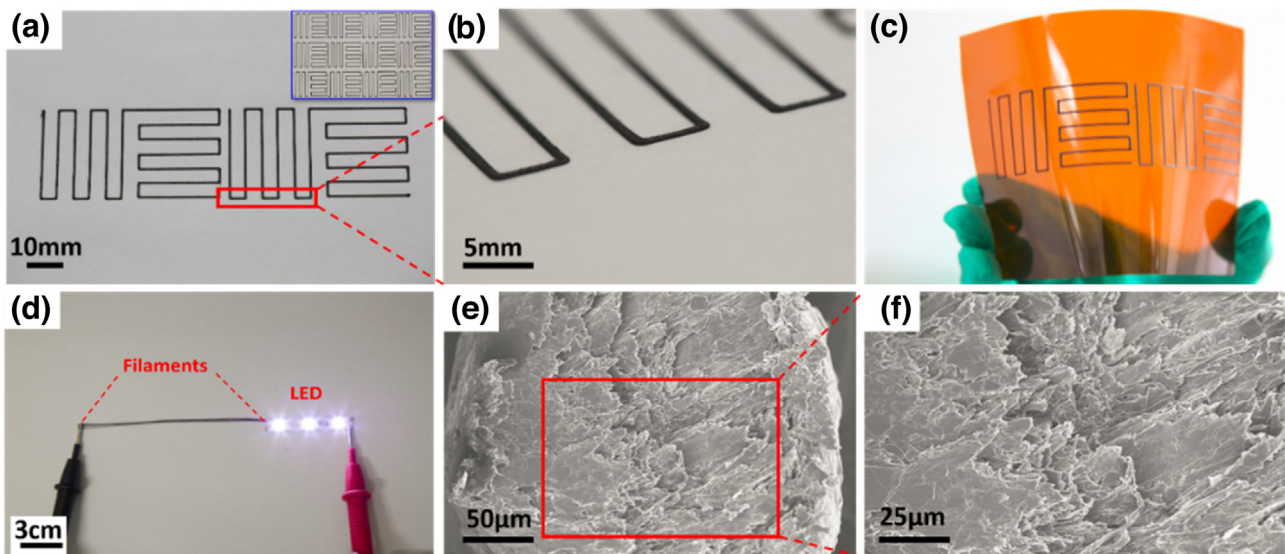


Fig. 5. (a) Two units of 3D printed paper-based flexible circuits pattern and the inset is an A4 paper with twelve units, (b) enlarged drawing of the selected part of (a), (c) 3D printed PI-based flexible circuits pattern, (d) LED circuit with a bunch of 3D printed filaments, (e) SEM cross section image of the filament from the 3D printer, (f) enlarged drawing of the selected part of (e).

6% weight ratio as the materials to print 2D and 3D structures so that the 3D printed products can maintain its flexibility.

3.3. Characterizations of 2D flexible circuits

The 2D flexible circuits are showed in Fig. 5. First, we use the Makerbot to design the 2D structure pattern, that is, the monolayer structure with the tetragonal lines. Then we use the paper as the substrate to print the flexible circuits. The temperature of the 3D printer was set to 210 °C, Fig. S3 shows the DSC spectra of the pure PLA and the PLA-graphene (6 wt%), from which we can see that the melting point of PLA is 154.3 °C. The addition of graphene increase the melt point and melt viscosity of PLA. Therefore the temperature of the 3D printer must high enough to assure the composite filament (1.75 mm) be smoothly extruded from the capillary nozzle. Fig. 5(a) shows two units of the designed pattern, in which we can see the clean neat lines with the same thickness. The width and the height of the lines are 800 μm and 100 μm , respectively. The inset is an A4 paper sized picture, on which 12 units are printed, all the units are of the same quality. The A4 paper sized pattern with 12 units were finished within 3 min. The video with the normal play speed (Movie S1) can show the printing speed when print the 2D flexible circuits. Fig. 5(b) enlarge the selected part in Fig. 5(a), it can be clear seen that the printing lines exhibit cuboid-like shape, and the composite circuits has a very good bonding force with the paper. Hence when the paper was bended, the composite circuits are bend just the same as the paper without any deformation or warping. It is worth to note that the corners of the pattern (Fig. 5(b)) are homogeneous as the other part, which means that the contact resistance of the corners will low enough to be ignored. We change the paper substrate to polyimide (PI) (Fig. 5(c)), which is transparent and has higher mechanical properties, and the surface of PI is much more smoother than that of paper. The printing lines on PI substrate also exhibit cuboid-like shape, just the same as the paper substrate. When the PI was bended, the composites circuits can keep sticking on the PI, indicating that the composite circuits can be well bonded with most flexible substrates. In order to illustrate the superior conductivity of the 3D printed composites filaments, a simple

LED circuit was set up (Fig. 5(d)). We inserted a bunch of 3D printed filaments in the circuit, and the LED can shine under the normal voltage (15 V). Movie S2 shows the process. This phenomenon further proves that the contact resistance of the filament can be ignored and the whole resistance of a bunch of 3D printed composites filaments is near equivalently to a single copper wire.

We particularly study the conductivity change of the composite from HAKKE mixing to 3D printing. PLA and graphene were melt blended in HAKKE mixer with different graphene ratio (2%, 4%, 6%, 8%), then the four groups of samples were fused suppressed into wafer samples with the radius of 1.5 cm and the thickness 1 mm. The four-probe method was used to measure the conductivities of the wafer samples. Meanwhile, the four groups of samples from HAKKE were extruded into the filaments with the diameter of 1.75 mm by a mini single screw extruder, and further extruded by 3D printer. The two-point method was used to measure the conductivity of the 1.75 mm filaments and the filaments from the capillary nozzle of 3D printer. Table S3 shows the results, the conductivities increase as the increase of graphene ratio no matter whether the wafer samples or the filaments samples. But we can clearly see that the overall conductivity of the 3D printed filaments is higher than that of the 1.75 mm filaments, and the overall conductivity of 1.75 mm filaments is higher than the wafer samples (3D printed filaments > 1.75 mm filaments > wafer samples). In other words, the conductivity of PLA-graphene composite will increase after every extrusion process. Fig. S2 shows the conductivity change trend. It is worth noting that the conductivity of PLA-graphene has a sharply increase from 4 wt% to 6 wt%, so we believe that the percolation threshold of r-GO to PLA is between 5% and 8%. We believe that the graphene has a process of orientation during the extrusion thus contributing to increase the conductivity of the composite. Fig. 5(e and f) shows the SEM cross section images of the filament from the capillary nozzle (3D printed filament), and the directional orientation structure can be clearly seen. The graphene sheets form the lamellar orientation feature, which confirming the fact that the orientation of graphene occurred during the extrusion process, thus increasing the conductivity of the composite.

Meantime, we have measured the conductivity change of the 3D printed filaments (diameter 0.4 mm) under the bending

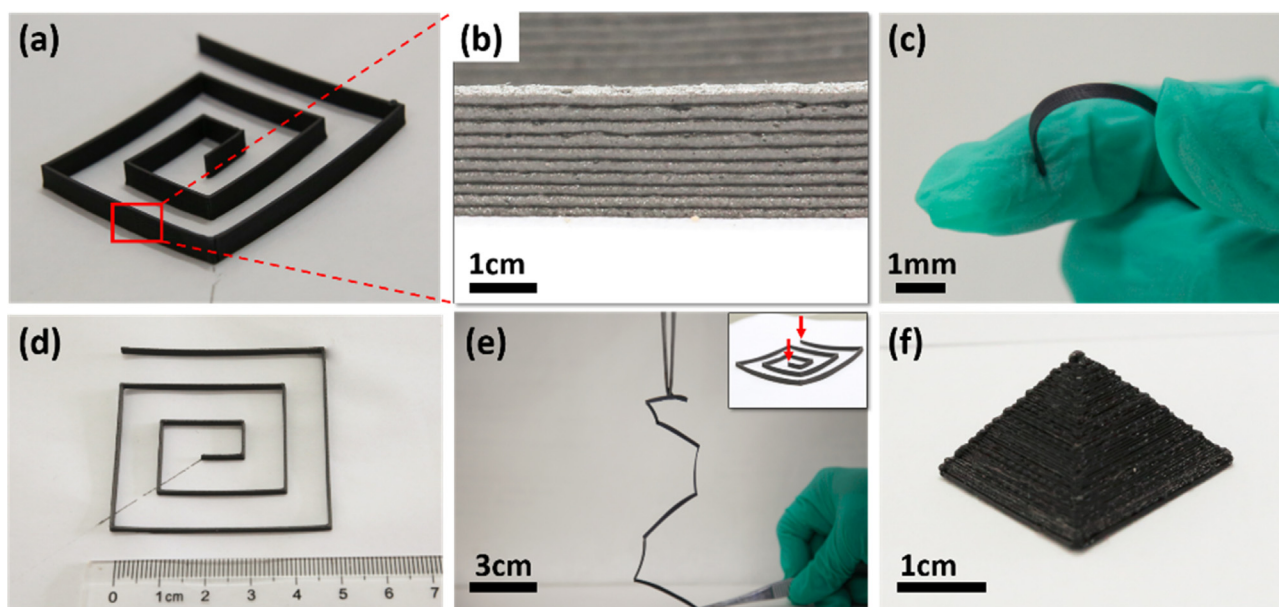


Fig. 6. (a) 3D printed flexible circuits, (b) enlarged drawing of the selected part of (a), (c) the bend of part of the 3D flexible circuits, (d) vertical view picture of the 3D flexible circuits and the measuring ruler, (e) fore and aft stretch (vertical direction) of the 3D flexible circuits, the inset are the schematic drawing for the places of clamps, (f) 3D printed mini pyramid.

(Fig. S4 and Table S4) and stretching (Fig. S5) states. The detailed experiment steps and the mechanism analysis of the observed phenomenon are in the supporting information. The results show that the composite circuits can keep its high conductivity under different bending states. And the conductivity of the filament will sharply decrease as the stretch process.

3.4. Characterization of 3D flexible circuits

We design and print three dimensional flexible circuits as shown in Fig. 6(a). The melted filament was cool down immediately after extruded through the nozzle without any shrinkage or extrusion swelling. The filaments diameters of all layers are range from 200 μm to 300 μm . The whole structure is strong enough to handle and stretch, and the surface of the structure is smooth. Fig. 6(b) is the enlarged picture of the selected part in Fig. 6(a), in which the 10 layers of the 3D flexible circuits are showed clearly, and the height of this 10 layers is 2.8 mm. Just as the 2D flexible circuits, the first layer of the 3D flexible circuit that stick to the paper is cuboid-like as well, because the height of the first layer is lower than other layers. The layers over the first one are all cylindrical filaments. The bond between the layers are very tight, indicating that the structure can keep a good mechanical properties in the vertical direction. Fig. 6(c) shows a section of 3D flexible circuits between the fingers. The bend shape between the fingers clearly shows the good flexibility of the 3D flexible circuits.

The measuring ruler in Fig. 6(d) shows the size of the square spiral 3D flexible circuits, the side length of the outer square is 5 cm. It can be easily calculated that the filament of every layer is 30 cm long, demonstrating that the filament can be homogeneously extruded from the nozzle without any break off. The surface of the 3D flexible circuits is very smooth and no burrs or flangings can be seen. This 3D structure is larger than any other 3D printed graphene composite reported [26]. In Fig. 6(e), We used tweezers to clamp the head and the end (the arrow mark places in the inset picture) of the 3D flexible circuits and stretch it along the vertical direction. Fig. S6 shows the gradual degree of stretch for 3D flexible circuits. No fracture occurred

during the whole stretch process, which further prove the good mechanical properties and flexibility of the 3D flexible circuits. We even print a mini sized hollow pyramid (Fig. 6(d)) to prove that this PLA-graphene composite can be used to print complex structure. The mechanical properties and the flatness of the pyramid are just the same as the square spiral. We believe that PLA own a better processability than other FDM materials like ABS or PP.[27] If the platform is large enough, this conductive PLA-graphene composite can be used to print any sized conductive structure, which will open a wide gate in the organic electronic fields.

3.5. Morphology of 3D printed products

The AFM and SEM were used to further analyze the microtopography of the 2D and 3D flexible circuits. The left image of Fig. 7(a) shows the SEM image of 3D printed cylindrical filament (one layer of the 3D flexible circuit) which exhibit uniform diameter, and the right image of Fig. 7(a) is the SEM image of the cuboid-like line of the 2D flexible circuit (Fig. 5(a and b)). On both surfaces, the lamelleted structure can be seen clearly, that's because the graphene sheets are homogenously dispersed and wrapped by the PLA and exposed on the surface, suggesting the high conductivity of the composite. It is interesting that the width of the 2D flexible circuit line is much longer than the diameter of the 3D printed filament, which corresponding to the fact in Fig. 6(b) that the first layer exhibits cuboid shape while the other layers are the normal filaments extruded from the nozzle of the 3D printer. We believe that it's duo to the difference of the surface tension between the substrate and the composite: for the first layer, when the melted filament extruded from the nozzle and come into contact with the surface of the substrate (paper or PI), it will have a certain degree of spread wetting process before cooling because of the higher surface tension of the substrate. For the second layer and above, similarly, due to the lower surface tension of the first layer, to wit, the composite, the melted filament can keep its shape until cooling. As thus, the broad platform of the first layer makes it offer a larger contact area to the second layer,

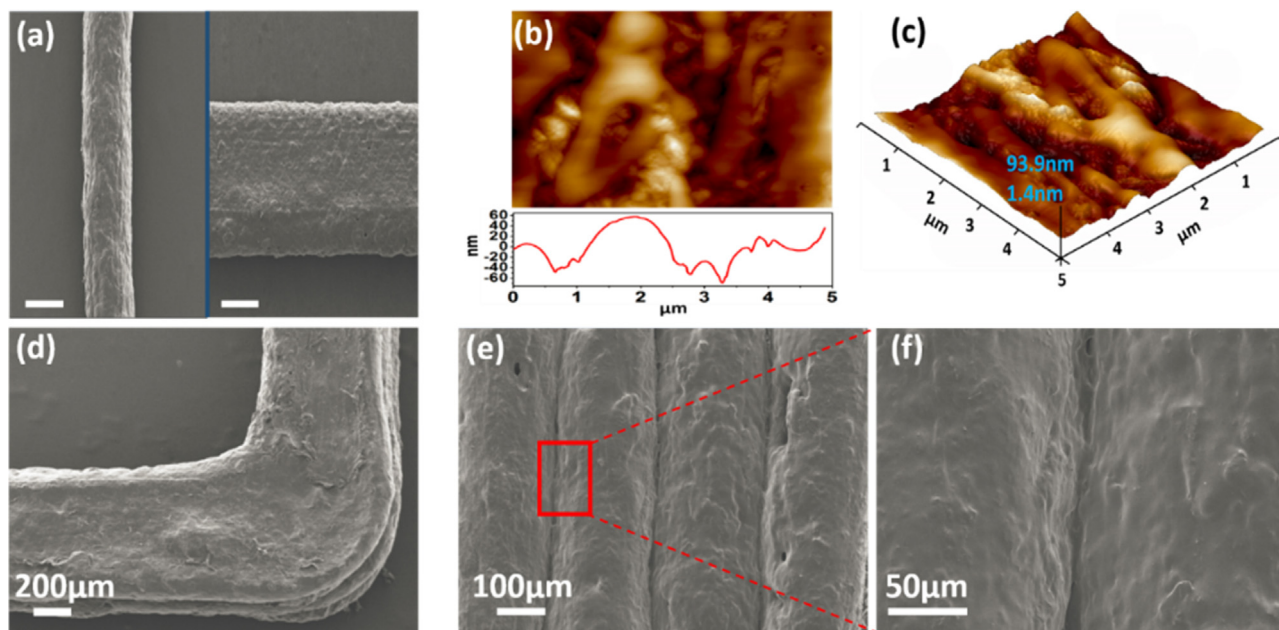


Fig. 7. (a) Left is the SEM image of 3D printed filament with the scale bar: 100 μm , the right is the line of 2D structure with the scale bar: 100 μm , (b) AFM topographic image of the 2D structure surface and the corresponding height profile, (c) three dimensional topographic image of Fig. 6(b), (d–f) SEM images of 3D structure from different angles (corner, lateral direction and the selected enlarged picture, respectively).

strengthening the cementation between the substrate and the 3D structure, and the mechanical properties in the vertical direction are also enhanced. In order to analyze the topographical microstructure of the extruded filaments and determine the mechanical properties, we selected some parts of the first layer and took some AFM images with the scope of $5\ \mu\text{m} \times 5\ \mu\text{m}$. Fig. 7(b) and (c) display one of the AFM images, height profile, and the corresponding three dimensional topographic image. Some drapes and fluctuations are showed under the high magnification times (Fig. 7(b)). The fluctuating height are within 70 nm basing on the horizontal line. Fig. 7(c) shows the rugged morphology clearly. We can calculate that the maximum height difference value is 92.5 nm, indicating that the surface of the filaments from 3D printer is very smooth, no big defects exist which will impact the mechanical properties.

We cut one corner part of the 3D flexible circuit, and got the top view SEM image (Fig. 7(d)), we can see a few layer from above. What counts is that the bonding surface between two layers are also have a certain degree of spread out thus forming a platform, just like the first layer, offering a substantial contact area for the cementation. Hence, the vertical mechanical properties of the 3D structure can be guaranteed. We also got the SEM image of 3D flexible circuit from the lateral direction (Fig. 7(e)) and the enlarged picture of its selected part (Fig. 7(f)). Fig. 7(e) clearly shows that the cementation between every two layers are very well, there is no gaps between the layers. From the enlarged picture (Fig. 7(f)) we can see that the two layer are fused with each other in the junction, further confirming that the 3D structure possess good mechanical properties.

4. Conclusions

Two-step reduced method was used to fabricate the high conductive graphene, the conductivity of which can reach to 600 S/cm. PLA was chosen to be the polymer substrate of the synthesized graphene, the graphene can be well dispersed in the PLA and has a strong interface bonding force with PLA. The melt blending method was used to mix the PLA and the synthesized graphene. The 3D print-used filaments were fabricated by melt extrusion, and the filaments can be smoothly extruded from the spray nozzle. The composite filaments from 3D printer exhibit the conductivity of 4.76 S/cm (6 wt%). 2D and 3D flexible circuits were printed rapidly, which exhibit smooth surface and superior mechanical properties. The PLA-graphene composite can be used to print any complex 3D structure, which will bring a promising vista in organic electronic fields.

Acknowledgements

Research Fund for the Doctoral Program of Higher Education of China (Grant No. 20110010110007) and National Natural Science Foundation of China (Grant No. 51173013 and No. 51573012) for the financial supports.

Appendix A. Supplementary data

Supplementary data associated with this article can be found, in the online version, at <http://dx.doi.org/10.1016/j.synthmet.2016.03.014>.

References

- [1] W. Putian, G. Jinbao, W. Huihui, Y. Zhang, J. Wei, J. Phys. Chem. C 113 (2009) 8118.
- [2] (a) W. Huihui, G. Jinbao, L. Jia, J. Wei, Carbon 49 (2011) 779; (b) J. Li, L. Liu, D. Zhang, D. Yang, J. Guo, J. Wei, Synth. Met. 192 (2014) 15.
- [3] B. Basnar, I. Willner, Small 5 (2009) 28.
- [4] J. Chang, C.K. Najeeb, J.H. Lee, J.H. Kim, Langmuir 27 (2011) 7330.
- [5] (a) M. Mionic, K. Pataky, R. Gaal, A. Magrez, J. Brugger, L. Forro, J. Mater. Chem. 22 (2012) 14030; (b) B.J. de Gans, P.C. Duineveld, U.S. Schubert, Adv. Mater. 16 (2004) 203; (c) M. Kuang, L. Wang, Y. Song, Adv. Mater. 26 (2014) 6950; (d) Z. Zhang, X. Zhang, Z. Xin, M. Deng, Y. Wen, Y. Song, Adv. Mater. 25 (2013) 6714; (e) S. Chen, M. Su, C. Zhang, M. Gao, B. Bao, Q. Yang, B. Su, Y. Song, Adv. Mater. 27 (2015) 3928.
- [6] (a) M.F. El-Kady, R.B. Kaner, Nat. Commun. 4 (2013) 1475; (b) H. Tian, C. Li, M.A. Mohammad, Y.L. Cui, W.T. Mi, Y. Yang, D. Xie, T.L. Ren, ACS Nano 8 (2014) 5883.
- [7] H. Tian, Y. Shu, Y.L. Cui, W.T. Mi, Y. Yang, D. Xie, T.L. Ren, Nanoscale 6 (2014) 699.
- [8] (a) A.A. Balandin, S. Ghosh, W. Bao, Nano Lett. 8 (2008) 902; (b) Y. Zhang, Y.W. Tan, H.L. Stormer, P. Kim, Nature 438 (2005) 201; (c) K.I. Bolotin, K.J. Sikes, Z. Jiang, M. Klima, G. Fudenberg, J. Hone, P. Kim, H.L. Stormer, Solid State Commun. 146 (2008) 351; (d) C. Lee, X. Wei, J.W. Kysar, H. James, Science 321 (2008) 385; (e) M.D. Stoller, S. Park, Y. Zhu, J. An, R.S. Ruoff, Nano Lett. 8 (2008) 3498.
- [9] (a) H. Wang, L.F. Cui, Y. Yang, H.S. Casalongue, J.T. Robinson, Y. Liang, Y. Cui, H. Dai, JACS 132 (2010) 13978; (b) R. Chen, T. Zhao, W. Wu, F. Wu, J. Li, R. Xu, H. Wu, H.M. Albishri, A.S. Al-Bogami, D.A. El-Hady, J. Lu, K. Amine, Nano Lett. 14 (2014) 5899.
- [10] (a) Y. Xie, Y. Liu, Y. Zhao, Y.H. Tsang, S.P. Lau, H. Huang, Y. Chai, J. Mater. Chem. A 2 (2014) 9142; (b) N. Jung, S. Kwon, D. Lee, D.M. Yoon, Y.M. Park, A. Benayad, Adv. Mater. 25 (2013) 6854.
- [11] (a) V.M. Oscar, J.P. Bosco, O. Ergen, H.I. Rasool, A. Fathalizadeh, M. Tosun, M. Crommie, A. Javey, H.A. Atwater, A. Zettl, Nano Lett. 14 (2014) 4280; (b) Z. Yin, J. Zhu, Q. He, Adv. Energy. Mater. (2014) 4.
- [12] (a) A.P.A. Raju, A. Lewis, B. Derby, R.J. Young, I.A. Kinloch, R. Zan, K.S. Novoselov, Adv. Funct. Mater. 24 (2014) 2865; (b) Y. Li, H. Yan, D.B. Farmer, X. Meng, W. Zhu, R.M. Osgood, T.F. Heinz, P. Avouris, Nano Lett. 14 (2014) 1573.
- [13] R. Raccichini, A. Varzi, S. Passerini, B.S. Affiliations, Nat. Mater. 14 (2014) 271.
- [14] (a) G.M. Gratson, M. Xu, J.A. Lewis, Nature 428 (2004) 386; (b) M. Campbell, D.N. Sharp, M.T. Harrison, Nature 404 (2000) 53; (c) B.H. Cumpston, S.P. Ananthavel, S. Barlow, Nature 398 (1999) 51.
- [15] (a) G. Comina, A. Suska, D. Filippini, Lab Chip 14 (2014) 2978; (b) N.T. Eigenfeld, J.M. Gray, J.J. Brown, G.D. Skidmore, S.M. George, V.M. Bright, Adv. Mater. 26 (2014) 3962; (c) A. Russo, B.Y. Ahn, J.J. Adams, E.B. Duoss, J.T. Bernhard, J.A. Lewis, Adv. Mater. 23 (2011) 3426; (d) J.J. Adams, E.B. Duoss, T.F. Malkowski, M.J. Motala, B.Y. Ahn, R.G. Nuzzo, J.T. Bernhard, J.A. Lewis, Adv. Mater. 23 (2011) 1335.
- [16] (a) S.Z. Guo, F. Gosselin, N. Guerin, A.M. Lanouette, M.C. Heuzey, D. Theriault, Small 9 (2013) 4118; (b) L.L. Lebel, B. Aissa, M.A.E. Khakani, D. Theriault, Adv. Mater. 22 (2010) 592.
- [17] (a) J.T. Muth, D.M. Vogt, R.L. Truby, Y. Menguc, D.B. Kolesky, R.J. Wood, J.A. Lewis, Adv. Mater. 26 (2014) 6307; (b) S.A. Morin, Y. Shevchenko, J. Lessing, S.W. Kwok, R.F. Shepherd, A.A. Stokes, G.M. Whitesides, Adv. Mater. 26 (2014) 5991; (c) S.W. Kwok, S.A. Morin, B. Mosadegh, J.H. So, R.F. Shepherd, R.V. Martinez, B. Smith, F.C. Simeone, A.A. Stokes, G.M. Whitesides, Adv. Funct. Mater. 24 (2014) 2180; (d) B. Mosadegh, P. Polygerinos, C. Keplinger, S. Wennstedt, R.F. Shepherd, U. Gupta, J. Shim, K. Bertoldi, C.J. Walsh, G.M. Whitesides, Adv. Funct. Mater. 24 (2014) 2163.
- [18] (a) A. Sutradhar, J. Park, D. Carrau, M.J. Miller, Comput. Biol. Med. 52 (2014) 8; (b) D. Maragiannis, M.S. Jackson, S.R. Igo, M.C. Su, W.A. Zoghbi, H.L. Stephen, J. Am. Coll. Cardiol. 64 (2014) 1066; (c) K.H. Herrmann, C. Gärtner, D. Güllmar, M. Kramer, J.R. Reichenbach, Med. Eng. & Phys. 36 (2014) 1373; (d) K.A. Simon, K.M. Park, B. Mosadegh, A.B. Subramaniam, A.D. Mazzeo, P.M. Ngo, G.M. Whitesides, Biomaterials 35 (2014) 259.
- [19] V. Queral, Fusion Eng. Des. 89 (2014) 2145.
- [20] O.K. Park, M.G. Hahm, S. Lee, H.I. Joh, S.I. Na, R. Vajtai, J.H. Lee, B.C. Ku, P.M. Ajayan, Nano Lett. 12 (2012) 1789.
- [21] C. He, L. Liu, Z. Fang, J. Li, J. Guo, J. Wei, Ultrason. Sonochem. 21 (2014) 542.
- [22] K.S. Novoselov, A.K. Geim, S.V. Morozov, D. Jiang, Y. Zhang, S.V. Dubonos, I.V. Grigorieva, A.A. Firsov, Science 306 (2004) 666.
- [23] J.M. Holden, P. Zhou, X.X. Bi, Chem. Phys. Lett. 220 (1994) 186.
- [24] J.I. Paredes, S. Villar-Rodil, P. Solis-Fernandez, A. Martinez-Alonso, J.M.D. Tascon, Langmuir 25 (2009) 5957.
- [25] J.Y. Sun, C. Keplinger, G.M. Whitesides, Z. Suo, Adv. Mater. 26 (2014) 7608.
- [26] A.E. Jakus, E.B. Secor, A.L. Rutz, S.W. Jordan, M.C. Hersam, R.N. Shah, ACS Nano 9 (2015) 4636.
- [27] X. Wei, D. Li, W. Jiang, Z. Gu, X. Wang, Z. Zhang, Z. Sun, Sci. Rep. 5 (2015) 11181.